

Mold Slag Entrainment Mechanisms in Continuous Casting Molds

Lance C. Hibbeler and Brian G. Thomas

The University of Illinois at Urbana–Champaign
Department of Mechanical Science and Engineering
1206 West Green Street (MC-244), Urbana, IL, USA, 61801
Phone: +1-217-339-6919
Email: lhibbel2@illinois.edu, bgthomas@illinois.edu

Key words: mold slag entrainment; inclusions; clean steel production; continuous casting

ABSTRACT

This article presents a comprehensive and critical review of slag entrainment in continuous casting molds. Entrainment is one of the main sources of inclusions in the final product, and so greatly harms clean steel production. By understanding the mechanisms that cause entrainment, the operating condition windows can be chosen to reduce defects. Nine mechanisms have been proposed over the last three decades, including top surface level fluctuations, meniscus freezing, vortexing, shear-layer instability, narrow face spout impingement upon the top surface, argon bubble interactions, slag crawling down the submerged entry nozzle (SEN), instability of the top-surface standing wave, and top surface “balding”. Previous investigations into each of these mechanisms are summarized, including both quantitative and qualitative descriptions of behavior. The quantitative models are combined to suggest best practices for clean steel production, but more work is needed to improve these predictions.

1. INTRODUCTION

Mold slag (or mold flux) entrainment, also called emulsification, engulfment, entrapment, or involvement, is characterized by mold powder being drawn into the molten steel pool inside a continuous casting mold. Mold slag entrainment can cause both surface and internal defects in the final product if the entrained droplets become trapped in the solidifying metal, and so is an important problem in the production of clean steel.

Slag entrainment has received much attention in the steel industry over the past three decades, resulting in several proposed mechanisms. Some of these mechanisms are relevant to other industrial processes involving fluid flow. The entrainment mechanisms reported in the literature fall into nine families: top surface level fluctuations, meniscus freezing, vortexing, shear-layer instability, narrow face spout impingement upon the top surface, argon bubble interactions, slag crawling down the submerged entry nozzle (SEN), instability of the top-surface standing wave, and top surface balding. Most mechanisms suggest a critical condition for entrainment that can be used as a practical evaluation of models of fluid flow in a caster, and also can be used together to define a safe operating window to avoid inclusions in the final product.

Many studies are based on measurements from room-temperature physical models, usually employing water and silicon oil as surrogate fluids for the molten steel and slag. These physical models are unable to meet all of the relevant similarity criteria simultaneously, so their results are difficult to interpret quantitatively. Typically, the bulk fluid flow pattern and top surface profile of the caster are captured in the water model by matching the Froude number and ensuring that the Reynolds number is in the turbulent regime¹. This requirement leaves the Weber number, mass density ratio, shear viscosity ratio, and other similarity criteria unsatisfied with most choices of fluids, so important phenomena such as interfacial tension effects are not reproduced properly. Additionally, the surrogate liquid properties can be changed with additives, which usually affect multiple properties, *e.g.*, an additive to change interfacial tension also may change the mass density, so it is difficult to isolate the individual contributions to the entrainment mechanisms. Any prediction of entrainment from a physical model must be interpreted skeptically since all of these phenomena inherently are important to entrainment.

The ever-advancing computer technology and computational fluid dynamics techniques have allowed numerical investigations of slag entrainment, though challenges related to turbulent and multiphase flows yet remain. The computational models discussed in this article include a variety of numerical techniques, turbulence models, and simulated physics. Computational modeling presents many challenges, such as grid-dependent errors and missing physics, but allows for precise control of physical properties; if done properly, this technique offers the potential for better insight into the underlying physics than physical models.

The previous works on this subject all agree that mold slag entrainment depends on the physical properties of the materials involved (especially mass density ρ , dynamic shear viscosity μ , and interfacial tension between fluids A and B Γ_{AB}); the slag/powder layer thickness h_u ; the flow system design (including SEN submergence depth h_{sen} , SEN geometry, and SEN port geometry); and the operating conditions (including casting speed V_C , strand/mold width w_{strand} and thickness t_{strand} , argon gas flow rate Q_{Ar} , and electromagnetic flow control).

Throughout this article, the subscript u refers to the *upper* fluid layer (melted mold powder or oil, *etc.*) and the subscript ℓ refers to the lower fluid layer (mold steel or water, *etc.*). Other symbols used in this article are the mass density ratio $r = \rho_u/\rho_\ell$, dynamic shear viscosity ratio $m = \mu_u/\mu_\ell$, velocity magnitudes V , flow rates Q , and the acceleration due to gravity g . The immersion depth of the SEN h_{SEN} is defined as the vertical distance between the the average position of top surface and the top edges of the ports.

2. ENTRAINMENT DOES NOT GUARANTEE INCLUSIONS

At the outset, it must be emphasized that entrainment is not detrimental to product quality unless the entrained particles become captured into the solidifying steel.

Studies have shown² that most slag droplets entrained into the molten steel are recaptured quickly back into the slag layer due to their buoyancy. A numerical study³ showed that particles may or may not become captured in an approaching dendritic solidification front depending on the particle diameter and composition, local crossflow velocity, steel composition, and other parameters. Downward flow velocities may exacerbate entrapment by suspending the rising particles and slag-coated argon bubbles in front of the solidifying interface⁴, which may explain why single-roll patterns are found to produce more slag entrainment defects⁵. This model³ has predicted that the flow pattern in the mold should deliver 70% of large (400 μm) particles to the slag layer, but less than 10% of small (10 μm to 40 μm) particles. The particle size produced by an entrainment mechanism, if known, is reported in this article for use with these entrapment models.

The capability of the liquid slag layer to absorb or reabsorb the inclusions that reach it depends greatly on the composition of the slag^{6,7}. Dynamic models have been constructed for solid⁸ and liquid⁹ particles to determine if a particle will enter the slag layer; the tendency to absorb decreases with decreasing inclusion particle diameter, decreasing wettability between the slag and particles, increasing interfacial tension, and increasing slag viscosity. However, as discussed in this article, the same properties that encourage inclusion removal often make entrainment more likely.

3. TOP SURFACE FLUCTUATIONS

The early studies of slag entrainment focused on the high-frequency, localized fluctuations of the top surface, likely because they are measurable in the plant and strongly correlate with the number of inclusion particles measured in the final product. However, numerical modeling^{10,11} has revealed how these fluctuations can entrain slag at the meniscus by exposing the dendritic solidification front at the top of the strand to the liquid slag and mold powder during a sudden drop in the liquid level. Figure 1 illustrates the sequence of events leading to entrainment by this mechanism. Although mold oscillation causes slight changes in the liquid level during each cycle, it is the transient changes in the flow pattern in the mold that cause the bigger level fluctuations that result in slag-entrainment defects. If the level fluctuations are severe enough relative to the slag layer thickness, this mechanism can even entrain solid mold powder. However, "severe enough" has not yet been quantified for either solid or liquid particle entrainment by this mechanism. In addition to turbulence and mold oscillations, the top surface level fluctuations can be caused by upstream flow control devices such as a slide gate¹² or stopper rod¹³, or shell bulging in secondary cooling.

Top surface fluctuations are associated with the turbulence of the liquid steel pool. The amplitude of the fluctuations increases with increasing casting speed^{14,15}, increasing SEN bore diameter¹⁶, increasing SEN port size¹⁶, aiming the SEN port angles more upwards^{15,16}, more shallow SEN immersion depth^{15,17}, and decreasing slab width^{15,18}. Fluctuations also increase with increasing argon flow rate^{15,16,19}, especially so with poor wettability between the argon and SEN refractory material¹⁹, but increasing the casting speed decreases the effect of the bubbles¹⁵. The effects of argon bubbles are discussed further in Section 8.

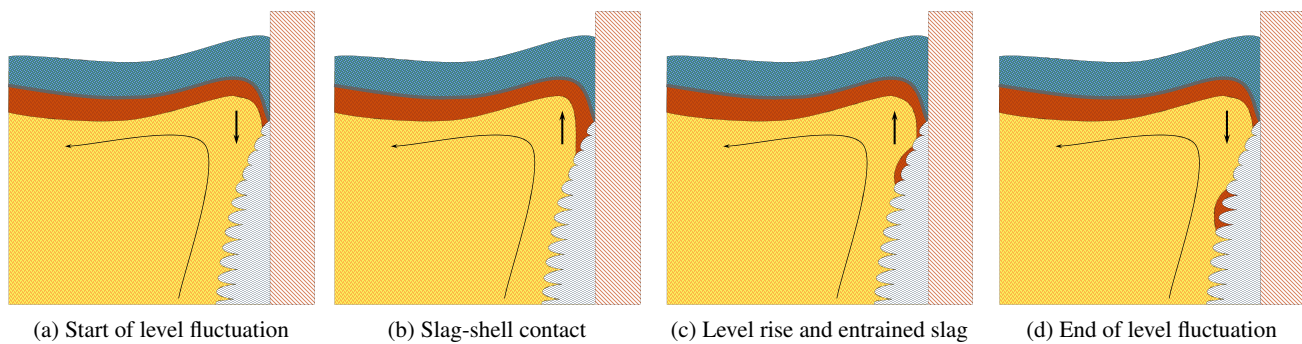


Figure 1. Entrainment by meniscus level fluctuation

The turbulence of the meniscus in water models has been observed, both by direct observation²⁰ and by measurements of turbulent kinetic energy²¹, to increase sharply with decreasing SEN immersion depth; the meniscus becomes quiet at sufficiently large immersion depths^{20,21,22}. The fluctuations in a water model²³ were suppressed with the proper combination of SEN immersion depth, argon flow rate, and SEN geometry, but all of these parameters depend on casting speed and mold width.

Fluctuations were observed in an actual caster²⁴ to have the same frequency and have about 70% of the amplitude of the applied mold oscillations. This percentage was observed to increase with casting speed²⁴, but a water model study²² showed that the fluctuation amplitude is independent of casting speed. The frequency of the fluctuations is the superposition of a low-frequency signal corresponding to the turbulent fluctuations of the SEN jet²² and a high-frequency signal^{22,25}, corresponding perhaps to a sloshing frequency. The mold has a natural frequency for high-amplitude level fluctuations due to gravity wave sloshing, which can be amplified by improper slide-gate dithering frequency¹². The higher-frequency fluctuations are damped more quickly with a slag layer than without¹³, emphasizing that models of fluid flow in a caster must include the slag layer to reproduce the flow patterns properly¹. Low-frequency fluctuations are generated by the steel jet wandering in the molten steel pool^{26,27}, whose frequencies f scale with the Strouhal number fh_{SEN}/V_C ²⁶. This jet wandering can produce transient surface velocities near 1 m/s²⁶.

Single-roll flow patterns are more susceptible to defects via this mechanism, and combinations of flow-control variables that produce continuously unstable complex flow patterns are worse²⁸. Electromagnetic forces offer another variable to control the flow pattern. Plant experiments using electromagnetic braking have reported decreases in level fluctuations and associated defects (cf. the review in the paper by Cukierski and Thomas²⁹). Other plant experiments have reported the use of traveling electromagnetic field stirring to control fluctuations and significantly reduce the number of defects¹⁴.

In double-roll flow patterns, many flow related phenomena, including level fluctuations, strongly correlate with the strength of the flow up the narrow face, discussed further in Section 7. One characterization of the effect of SEN and mold geometry on the strength of flow up the narrow face is the “ F Value,”¹⁵ defined as

$$F = \rho_l Q_{SEN} V_{coll} \frac{1 - \sin(\theta_{coll})}{4h_{coll}}, \quad (1)$$

where Q_{SEN} is the flow rate through the SEN. The jet impinges onto the narrow face with collision speed V_{coll} and angle below horizontal θ_{coll} , and h_{coll} is the depth of the impingement point below the top surface, as illustrated in Figure 2. The collision speed increases with increasing casting speed^{15,20} and decreasing slab width²⁰. The depth of the impingement point h_{coll} increases with increasing slab width²⁰, increasing SEN immersion depth²⁰, and decreasing argon gas flow rate¹⁶.

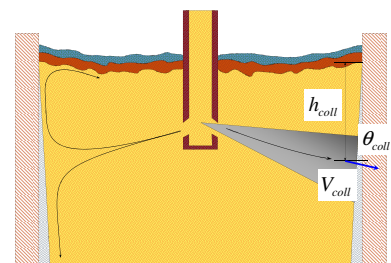


Figure 2. F Value model description

Plant experiments showed that keeping the “ F Value” between 3 N/m and 5 N/m¹⁵ (grade not given), or between 2 N/m and 3 N/m³⁰ for a low-carbon aluminum-killed steel results in slabs with good surface quality^{14,31}. Considering that the surface velocity $V_{surface}$ in m/s is related to level fluctuation amplitude δ in mm by $V_{surface} = \delta/35$, and that the amplitude of level fluctuations increases linearly with F as approximately $\delta = 3F$ ^{14,15}, these recommendations translate to keeping the surface velocity between 0.26 m/s and 0.43 m/s. The lower limit likely is related to defects caused by meniscus freezing, discussed further in Section 4, and the upper limit likely is related to interfacial shear phenomena, discussed in Sections 6 and 7.

4. MENISCUS FREEZING AND HOOK FORMATION

A mechanism for the entrainment of slag and inclusion particles to form surface defects is illustrated in Figure 3, which shows a slag particle being captured by a hook. The root cause of hook formation is freezing of the meniscus^{32,33} due to insufficient heat delivered to the meniscus region, particularly near the narrow face where temperatures tend to be lowest. The frozen meniscus can extend into the melt where it captures rising bubbles, slag droplets, or solid inclusions. Additionally, when the molten steel supported above the frozen meniscus overflows, it can carry and entrap slag into the space just above the hook. Hooks can be prevented by increasing superheat, aiming the SEN port angles more upward, or increasing the flow velocity, all of which increase the heat supplied to the meniscus region.

Flow conditions such as those produced by a shallow SEN may produce excessive meniscus velocities, which increase surface turbulence, leading to instability, entrainment, and uneven mold powder distribution, as discussed in Section 3. However, too large of an SEN immersion depth can result in shell thinning below mold exit²⁰, top surface freezing (“bridging”), and hook formation. Electromagnetic flow control systems have been used¹⁴ to increase flow velocities at lower casting speeds and higher strand widths to avoid hook formation. This meniscus freezing phenomenon imposes a lower limit on surface velocities, perhaps corresponding to that of the flow criteria discussed in Section 3.

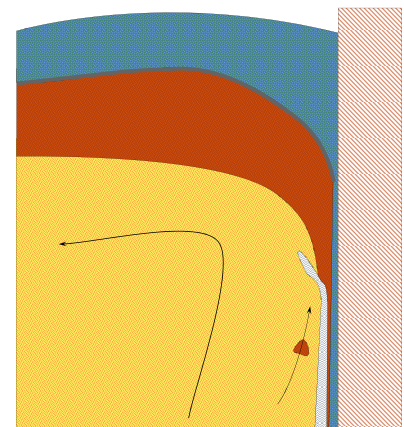
5. VORTEX FORMATION

Flow past bluff bodies such as an SEN can cause periodic shedding of vortices in the wake of the object, known as a von Kármán vortex street. These vortices can pull slag down into the molten steel, as shown in Figure 4. Any asymmetry between the sides of the mold in the flow pattern, including those caused by turbulent flow, can result in the formation of vortices around the SEN in one of four locations near the SEN^{17,34}, although vortex formation does not guarantee slag entrainment. Strong vortices that form and stay near the SEN can entrain slag that becomes entrapped in the solidifying dendrites on the wide face, resulting in increased sliver defects in the center of slabs²⁰. As shown in Figure 4c, vortices also may pull a funnel of slag deep enough into the molten steel pool such that the jet leaving the SEN breaks apart the tip of the vortex^{34,35,36,37}, transporting droplets of slag anywhere in the molten steel pool.

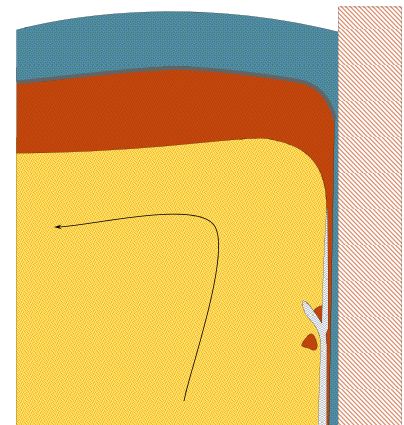
Asymmetric flow is reported to increase the frequency, depth, and size of the vortices³⁸. Asymmetric flow in the mold is caused by SEN clogging^{21,39}, asymmetric flow across the bottom of the tundish^{40,41}, stopper-rod misalignment^{4,34,42}, use of a slide-gate mechanism to control throughput^{43,44}, turbulent fluctuations even though the time-averaged flow field is symmetric^{34,42}, and other random asymmetries, such as coalescence of argon bubbles in the SEN sending a large argon bubble out of one port and not the other^{4,19}. The tendency for asymmetric flow was found to increase with increasing strand width, owing to the high throughput and a larger possible difference between impingement points on opposing narrow faces²⁰.

Vortices always are observed to form on the weaker (leeward) side of the flow, *i.e.*, in the wake of the SEN^{17,34,35,36,37,38,45,46}. Vortex depth increases with increasing top surface velocity^{36,45}. Vortex diameter increases with increasing SEN misalignment in either the width³⁶ or the thickness³⁷ directions. Vortex formation frequency increases with increasing SEN flow rate^{20,35,37,45}, increasing SEN misalignment^{36,37}, aiming the SEN port angles more upward^{35,37}, and increasing strand width^{17,20}. Vortex formation frequency also increases with more shallow SEN immersion depths^{17,20,35}, and there is a critical immersion depth that suppresses vortex formation (100 mm in the water model)³⁵. Vortex formation can be caused by misaligned stopper rods^{34,42}. Vortex formation also is a function of SEN geometry^{17,20}; vortex formation was reduced by keeping the ratio of the SEN inner diameter to the hydraulic diameter of the SEN ports greater than 1.1²⁰. The lifetime/duration of a vortex varies, but it eventually will be damped out by viscous dissipation or changing flow characteristics^{35,45}.

Vortex formation needs both rotational flow in the plane of the top surface (from asymmetric flow), and a downward-pulling sink³⁸. In double-roll flow patterns, the sink momentum is created where the opposing rolls meet near the center of the mold^{38,45}. Vortices were observed on the slower side of the mold moments after a peak in velocity on the opposite side⁴⁵. A



(a) Hook formation and rising particle



(b) Slag entrapment on back of hook and particle capture

Figure 3. Entrainment by hooks

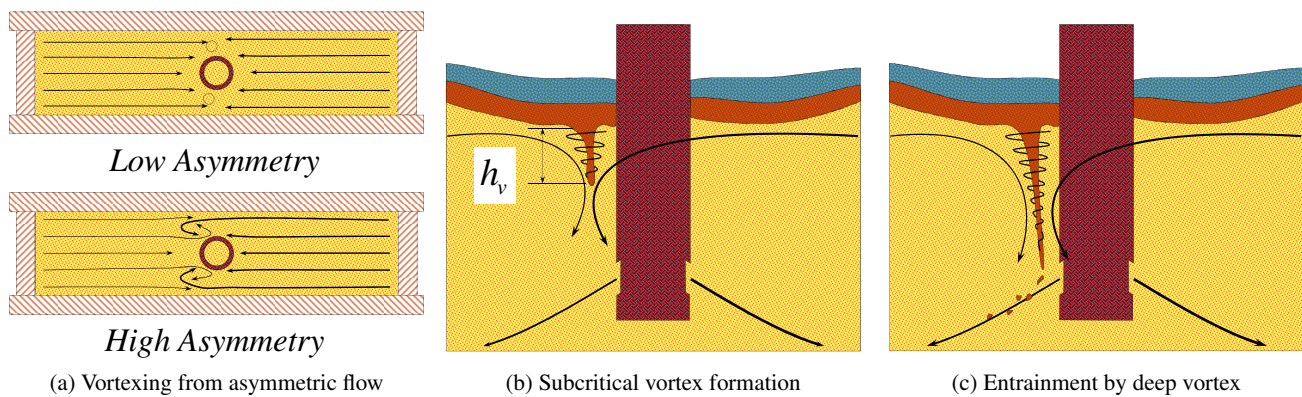


Figure 4. Entrainment by von Kármán vortex formation

sudden jump in downward velocity pulls the vortices deeper into the molten steel pool, enabling the jet to entrain slag from the tip of the funnel³⁵. Increasing the casting speed increases downward velocities and makes vortices more likely to form³⁶. A critical jump in downward velocity of 86 mm/s was observed to be needed before a vortex will form; above this limit, the occurrence frequency increases with further increases in the velocity jump³⁵. A maximum velocity for vortex formation also was observed, because excessive velocities cause the meniscus to become too oscillatory and turbulent to allow for the formation of vortices^{35,45}. However, meeting a critical surface velocity or flow rate criterion does not guarantee vortex formation¹⁷, and furthermore, the presence of a vortex does not necessarily mean that slag will be entrained into the melt³⁵.

The direction of rotation of the vortices depends on the side of the SEN by which the vortex forms, but has no apparent bearing on entrainment¹⁷. Vortices were observed to form both one at a time and in pairs^{17,35}. With a double-roll flow pattern, vortices formed within about 30 mm of the SEN outer wall and traveled outward to the narrow faces³⁵. Single-roll flow patterns, caused by shallow SEN immersion depths and wider strand widths, also suffer from vortices, but they form near the narrow faces instead of by the SEN³⁸.

Computational models have reported that vortices cannot occur with perfectly symmetric mold and SEN geometry and symmetric steady-state flow conditions^{36,47}, regardless of the mesh size and turbulence model⁴⁷. Realistic flow conditions, however, always produce transient asymmetries. In general, the more misaligned the SEN, the more asymmetric the flow pattern in the mold and the larger the vortex diameter^{36,37}. However, the amount of misalignment does not change the downward velocity that helps vortex formation³⁶.

Attempts to suppress vortex formation with flat fins protruding out of the SEN towards the narrow faces met with little success; vortex size and formation frequency remained unchanged, but the formation location moved away from the SEN to the tips of the fins²⁰. Inserting fins that block the flow from one half of the mold to another entirely suppresses vortex formation³⁸. Argon flow rates with more than 10% gas fraction induce buoyancy forces that can decrease the downward velocity near the SEN and prevent vortex formation, but that much argon reinforces asymmetric flow³⁶ and also can trigger some of the argon-related entrainment mechanisms discussed in Section 8. Electromagnetic flow control systems can be used to control flow asymmetry and effectively suppress vortex formation^{36,46}, but the flow control system settings depend on the SEN geometry⁴⁶. Use of both argon gas and electromagnetic flow control systems together can be effective in suppressing vortex formation for a given set of mold and SEN geometry³⁶.

Vortex formation frequency f_v (vortices per minute) was observed in water models¹⁵ to increase with increasing F value given by Equation (1), according to $f_v = \frac{3}{2}F - 10$ at maximum (for $F > 7$) and $f_v = \frac{1}{2}F$ on average. Another water model study³⁵ reported no vortex formation below an SEN flow rate of $Q_{SEN} = 35$ L/min, and above this limit the formation frequency increased with flow rate at about $Q_{SEN}/20$, where the slope depends on the properties of the slag (oil) layer.

A water model study⁴⁸ determined the SEN port velocity at which slag is entrained $V_{port,crit}$ to be

$$V_{port,crit} = \sqrt{g w_{strand} (1 - r) (c_1 + c_2 m)}, \quad (2)$$

where w_{strand} is the strand width, and the constants were fit as $c_1 = 0.1$ and $c_2 = 0.009167$ for 0 mm deep SEN wells and $c_1 = 0.35$ and $c_2 = 0.01833$ for 10 mm and deeper SEN wells. Another water model study³⁵ proposed a critical surface velocity of

0.3 m/s to form vortices, and the depth of a vortex h_v may be predicted by

$$h_v = \frac{V_{mc}^2}{g} \frac{1}{1-r} + c \left(\frac{\Delta V_s^2}{g} \frac{r}{1-r} \right)^{0.55} \quad (3)$$

where V_{mc} is the surface velocity (specifically halfway between the narrow faces, halfway between the SEN outer wall and the wide face, and 10 mm below the slag-metal (oil-water) interface), ΔV_s is the sudden change in vertical velocity that accompanies vortex formation (specifically 10 mm away from the SEN, halfway between the wide faces, and 50 mm below the slag-metal (oil-water) interface), and $c = 0.0562 \text{ m}^{0.45}$ is a constant with all other quantities in m-kg-s units. To avoid entrainment by this mechanism, the SEN immersion depth should be greater than the vortex depth³⁵.

The amount of slag entrained by vortices was measured experimentally^{49,50} for molten steel and several slags. This prediction of entrained mass can be used to predict particle diameter as

$$d = \sqrt[3]{\frac{6}{\pi} \frac{1}{\rho_u} \left(\frac{c}{\mu_u^{0.255} \Gamma_{ul}^{2.18}} \right)} \quad (4)$$

where $c = 3.057 \text{ kg}^{3.435} \cdot \text{m}^{-0.255} \cdot \text{s}^{-4.615}$ is a constant, μ_u is the slag viscosity in Pa-s, and Γ_{ul} is the interfacial tension in N/m, to give the mass (the term in parentheses) in kg. Slags with higher viscosity and higher interfacial tension yield smaller amounts of entrained slag.

6. SHEAR-LAYER INSTABILITY

The interface between two density-stratified fluids with relative motion will become unstable with a sufficiently large difference in velocity. A theoretical condition for this instability was first explored by Helmholtz⁵¹ in two dimensions for the interface between two inviscid, irrotational, and incompressible fluids in an infinite domain. The Helmholtz model did not include the effect of interfacial tension and so predicted instability at all velocity differences; this deficiency was resolved by Kelvin⁵². Most studies of slag entrainment have identified this phenomenon, known as Kelvin–Helmholtz instability (KHI), as a cause of mold slag entrainment, as shown in Figure 5. This shear instability mechanism is most likely to occur halfway between the narrow face and the SEN where the horizontal surface velocity is largest.

KHI is a fundamental hydrodynamic phenomenon and has received considerable treatment over the last 145 years. This phenomenon is found throughout nature, including ocean waves and clouds. A small perturbation to the interface between the two fluids grows without bound, *i.e.*, the interface becomes unstable, when the velocity difference between the fluids ΔV is greater than

$$\Delta V_{\text{instability}}(\lambda) = \sqrt{\left(\frac{\lambda}{2\pi} g (\rho_\ell - \rho_u) + \frac{2\pi}{\lambda} \Gamma_{ul} \right) \left(\frac{1}{\rho_u} + \frac{1}{\rho_\ell} \right)}, \quad (5)$$

where the perturbation to the interface has wavelength λ . Equation (5) is the result of a linear stability analysis and predicts only the transition from a stable interface to an unstable interface; it says nothing about the nature of the system once the interface has become unstable. The minimum velocity difference for instability predicted by this model is

$$\Delta V_{\text{crit}} = \sqrt[4]{4g (\rho_\ell - \rho_u) \Gamma_{ul} \left(\frac{1}{\rho_u} + \frac{1}{\rho_\ell} \right)^2}, \quad (6)$$

which occurs at the capillary wavelength λ_c ,

$$\lambda_c = 2\pi \sqrt{\frac{\Gamma_{ul}}{g (\rho_\ell - \rho_u)}}, \quad (7)$$

where the effects of interfacial tension and gravity are balanced.

An alternative prediction⁵³ of the Kelvin–Helmholtz instability for finite layer thickness, inviscid fluids, and zero interfacial tension gives a critical velocity of

$$\Delta V_{\text{crit}} = \sqrt{g (\rho_\ell - \rho_u) \left(\frac{h_u}{\rho_u} + \frac{h_\ell}{\rho_\ell} \right)}, \quad (8)$$

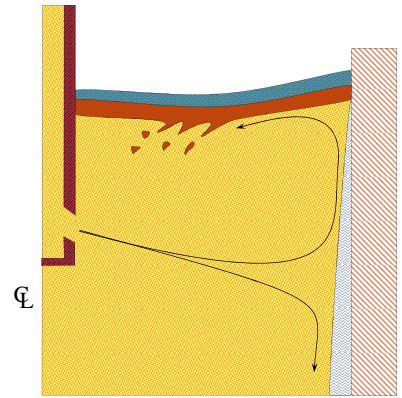


Figure 5. Shear-layer instability

where h_u and h_l are the thicknesses of the upper and lower layers. The validity of Equation (8) was confirmed in experiments⁵⁴ of a rotating covered trough for low-viscosity oils and low-frequency perturbations where interfacial tension is not dominant. The Kelvin–Helmholtz theory was generalized⁵⁵ to include the effects of interfacial tension, viscosity, and finite layer thickness. The prediction of critical velocity is

$$\Delta V_{\text{instability}}(\lambda) = \sqrt{\left((\rho_l - \rho_u)g \frac{\lambda}{2\pi} + \Gamma_{ul} \frac{2\pi}{\lambda} \right) \frac{(\mu_l \coth(\frac{2\pi}{\lambda}h_l) + \mu_u \coth(\frac{2\pi}{\lambda}h_u))^2}{(\rho_u \coth(\frac{2\pi}{\lambda}h_u) (\mu_l \coth(\frac{2\pi}{\lambda}h_l))^2 + (\rho_l \coth(\frac{2\pi}{\lambda}h_l) (\mu_u \coth(\frac{2\pi}{\lambda}h_u))^2)}. \quad (9)$$

This prediction of instability may not be valid for small layer thicknesses because the no-slip condition at the walls was not satisfied in the derivation of Equation (9). If the layer thicknesses become very large, the critical velocity is

$$\Delta V_{\text{crit}} = \sqrt[4]{4g(\rho_l - \rho_u)\Gamma_{ul} \frac{(\mu_l + \mu_u)^4}{(\rho_u \mu_l^2 + \rho_l \mu_u^2)^2}}, \quad (10)$$

which occurs at the same minimum perturbation wavelength as the Kelvin-Helmholtz inviscid model, Equation (6). The viscous solution produces a *lower* critical velocity than the inviscid solution; this counter-intuitive result is due to the additional momentum transfer caused by shear stresses. Equation (10) reduces to Equation (6) when the kinematic shear viscosities (μ/ρ) are equal in the two fluids, or when the density ratio equals the viscosity ratio⁵⁵. Letting the viscosities approach zero in the development of Equation (9) gives⁵⁵ a critical velocity of

$$\Delta V_{\text{instability}}(\lambda) = \sqrt{\left(\frac{\lambda}{2\pi}g(\rho_l - \rho_u) + \frac{2\pi}{\lambda}\Gamma_{ul} \right) \left(\frac{1}{\rho_u \coth(\frac{2\pi}{\lambda}h_u)} + \frac{1}{\rho_l \coth(\frac{2\pi}{\lambda}h_l)} \right)}. \quad (11)$$

As λ becomes large in Equation (11), Equation (8) is recovered exactly. Theoretical analysis⁵⁵ shows that the “most dangerous” three-dimensional perturbation to the interface is in fact the two-dimensional case considered in this section.

The stability of the interface is not affected by a magnetic field directed transverse to the flow^{56,57}, *i.e.*, DC electromagnetic flow control. A magnetic field applied parallel to the flow direction stabilizes the interface analogous to interfacial tension⁵⁶. Numerical studies of a continuous caster⁵⁷ that included interfacial tension and induced current effects from the finite-conducting steel shell showed that the parallel magnetic field adds to the effect of interfacial tension and damps out the instability flow structures, but does not affect the critical interface velocity.

7. UPWARD FLOW IMPINGING UPON THE TOP SURFACE

The upward spout along the narrow faces resulting from a double-roll flow pattern may cause slag entrapment in either a dragging⁵⁸ or cutting⁵⁹ fashion, as illustrated in Figures 6a and 6b. This is an example of shear-layer instability where the additional geometric aspects of the flow render the Kelvin-Helmholtz theory inapplicable.

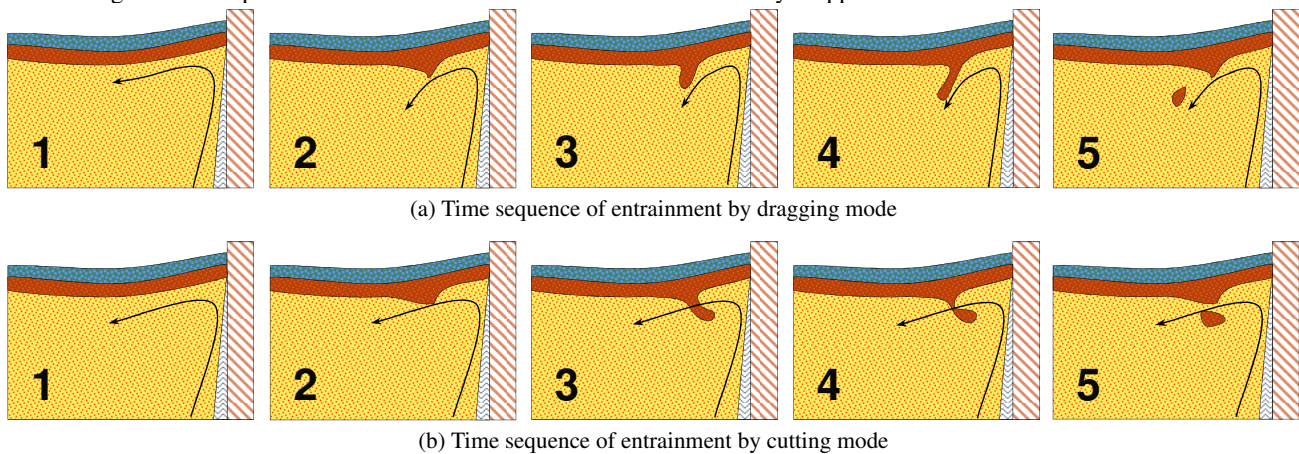


Figure 6. Entrainment by impinging flow upon the top surface

The first model of slag entrapment⁶⁰ proposed that entrapment occurs when the kinetic energy of a circular slag particle with diameter d exceeds the energy cost to form the particle surface and work done by the buoyancy force through a distance of

one-half the particle diameter, or

$$\frac{1}{2}\rho_u \frac{\pi d^3}{6} V^2 \geq \pi d^2 \Gamma_{ul} + g(\rho_\ell - \rho_u) \frac{\pi d^3}{6} \frac{d}{2}. \quad (12)$$

Taking the equality in Equation 12 and minimizing with respect to the particle diameter gives a critical surface velocity of

$$V_{\text{crit}} = \sqrt[4]{48} \sqrt[4]{\frac{g\Gamma_{ul}}{\rho_\ell}} \sqrt[4]{\frac{1}{r^2} - \frac{1}{r}}, \quad (13)$$

and accompanying particle diameter of

$$d = \sqrt{12} \sqrt{\frac{\Gamma_{ul}}{g(\rho_\ell - \rho_u)}}. \quad (14)$$

An extension⁶¹ of this first work includes the work done by the weight of the slag particle during a top surface level fluctuation with amplitude δ , *i.e.*, the term $g\rho_u \frac{\pi d^3}{6} (\delta - d)$ is included in the right side of Equation (12), giving a critical velocity of

$$V_{\text{crit}} = \sqrt{\sqrt{48} \sqrt[4]{\frac{g\Gamma_{ul}}{\rho_\ell}} \sqrt{\frac{1}{r^2} - \frac{3}{r}} - 2g\delta}, \quad (15)$$

which is limited to slags with density less than 1/3 that of steel. Another proposed criterion for entrainment¹⁶ is that the radius of curvature of the interface is smaller than produced droplet radius, giving the critical interface velocity of

$$V_{\text{crit}} = \sqrt{8} \sqrt[4]{\frac{g\Gamma_{ul}}{\rho_\ell}} \sqrt[4]{1-r}, \quad (16)$$

and droplet diameter of

$$d = 2 \sqrt{\frac{\Gamma_{ul}}{g(\rho_\ell - \rho_u)}}. \quad (17)$$

An oil-and-water physical model study⁶² used a submerged rotating cylinder to duplicate the flow field caused by the narrow-face spout. The proposed criterion for entrainment is a critical capillary number as a function of the ratio of kinematic shear viscosities,

$$V_{\text{crit}} = \frac{\Gamma_{ul}}{\mu_\ell} \left(c_1 + c_2 \frac{\mu_u/\rho_u}{\mu_\ell/\rho_\ell} \right) \quad (18)$$

where $c_1 = 2.8 \times 10^{-3}$ and $c_2 = 3 \times 10^{-6}$ are fitting constants.

An oil-and-water physical model study⁵⁹ reported a critical surface velocity of 0.116 m/s for this mechanism, which motivated a later study⁵⁸ that proposed the relation

$$V_{\text{crit}} = 3.065 \frac{\Gamma_{ul}^{0.292} g^{0.115} (\rho_\ell - \rho_u)^{0.215} \mu_u^{0.231}}{h_u^{0.356} \rho_u^{0.694} \mu_\ell^{0.043}} \quad (19)$$

for the critical velocity. Equation (19) was fit to measurements of an oil-and-water apparatus that used a submerged hose aimed at a wall to create the upward impinging flow pattern. The exponents in this model appear to be reasonable given the theoretical developments discussed in this section. The quantitative predictions of this model are reasonable for a steel-slag system, and the qualitative behavior is clear: entrainment occurs more easily with smaller interfacial tension, smaller slag viscosity, and larger liquid slag layer thickness h_u . The measured critical velocities were sensitive to the interfacial tension, but the density and surface tension were changed together using additives⁵⁸. Several droplets were entrained by the shearing flow, and the first entrained droplet always was the largest, with the diameter given by

$$d = 0.534 \frac{\Gamma_{ul}^{0.693} \mu_u^{0.114}}{g^{0.564} (\rho_\ell - \rho_u)^{0.130} \rho_u^{0.306} \mu_\ell^{0.372}}. \quad (20)$$

This study was repeated⁶³ with a wider range of properties and more controlled flow patterns and reported similar trends except for the effect of slag layer thickness; the difference might be due to variations in the angle of attack of the water jet. The

important parameters for entrainment by this mechanism are, in order: interfacial tension, mass density difference, dynamic shear viscosity, and slag layer thickness.

A similar entrainment mechanism occurs in ladle metallurgy. Combined oil-and-water experiments^{64,65} and multiphase numerical models⁶⁶ of a system that creates flow patterns similar to those found in continuous casting showed that shear-layer (Kelvin–Helmholtz) instability is the dominant mechanism for entraining slag in ladles. The shear flow first forms a “lip” at the interface that grows into a “ligament,” which at higher velocities breaks apart into droplets of various sizes. Using a higher-viscosity oil makes these ligaments thicker. This chain of events was observed to be periodic, with a period of 300 ms to 350 ms for the oils and velocities considered. Both the physical and numerical models showed that the velocities in the oil layer are about an order of magnitude smaller than the velocities in the water, indicating that the transfer of momentum by shearing stresses across the interface is small. The critical surface velocity was reported as about 0.26 m/s.

An oil-and-water physical model study⁶⁷ of slag entrainment in ladles found that entrainment occurs at a critical velocity of 0.233 m/s, which motivated the entrainment criterion of a critical density-modified Weber number of 12.3, giving critical velocity prediction of

$$V_{\text{crit}} = \sqrt{12.3} \sqrt[4]{\frac{g\Gamma_{u\ell}}{\rho_{\ell}}} \sqrt[4]{1-r}, \quad (21)$$

Some researchers⁶³ have suggested that such simple Weber-number relationships cannot make accurate predictions in systems as complicated as a continuous casting mold. This statement likely is true and the original researchers made a serendipitous choice with the Weber number. This critical value of 12.3 for the Weber number $We_{\text{crit}} = \rho_u V_{\text{crit}}^2 L / \Gamma_{u\ell}$ may be explained by assuming that the shear-layer instability mechanism causes the entrainment. Taking the critical velocity from the Kelvin–Helmholtz theory (Equation (6)) and one-half of the capillary wavelength (Equation (7)) as the characteristic velocity and length, the critical Weber number is $We_{\text{crit}} = 2\pi(1+r)$; using a density ratio of 0.98, typical for oil and water (property values not given in the original reference), this expression evaluates to 12.4. For density ratios appropriate for slag-and-steel systems this critical Weber number is about 8 to 9.

A theoretical model of the balance between inertia, interfacial tension, and buoyancy at the slag-steel interface in a ladle gives the critical surface velocity⁶⁸ as

$$V_{\text{crit}} = \sqrt[4]{\frac{128}{3} \cos(\alpha)} \sqrt[4]{\frac{g\Gamma_{u\ell}}{\rho_{\ell}}} \sqrt[4]{\frac{1}{r^2} - \frac{1}{r}}, \quad (22)$$

where α is the angle between the interface and the direction of gravity. The diameter of the corresponding droplet size is

$$d = \sqrt{\frac{6}{\cos(\alpha)}} \sqrt{\frac{\Gamma_{u\ell}}{g(\rho_{\ell} - \rho_u)}}. \quad (23)$$

This model should be applied with care for nearly horizontal interfaces.

8. ARGON BUBBLE INTERACTIONS

The interaction of the molten steel and slag flows with argon gas bubbles leads to another family of entrainment mechanisms. Argon gas usually is fed into the SEN to help prevent SEN clogging, which causes problems with nonmetallic inclusions and asymmetric fluid flow²¹. Argon bubbles also add a buoyancy force to the steel flow that lifts the jet upwards towards the steel/slag interface^{16,23,69}, changing the flow pattern. Argon gas can alleviate some problems, such as meniscus freezing (Section 4) and vortex formation (Section 5), but can aggravate other entrainment mechanisms, such as the top surface fluctuations (Section 3). Additionally, nonmetallic inclusions and slag can adhere to the surface of argon bubbles⁵⁹, leading to large defects if entrapped in the final product.

A water model study⁵⁹ showed that gas bubbles flowing out of the SEN can form a foam with the oil (slag) layer, illustrated in Figure 7a. This foam then can adhere to and crawl down the outside of the SEN and break apart in the jet, which entrains large amounts of slag, as shown in Figure 7b. The formation of this slag foam leads to entrainment defects despite small mold surface velocity and level fluctuations⁵⁹.

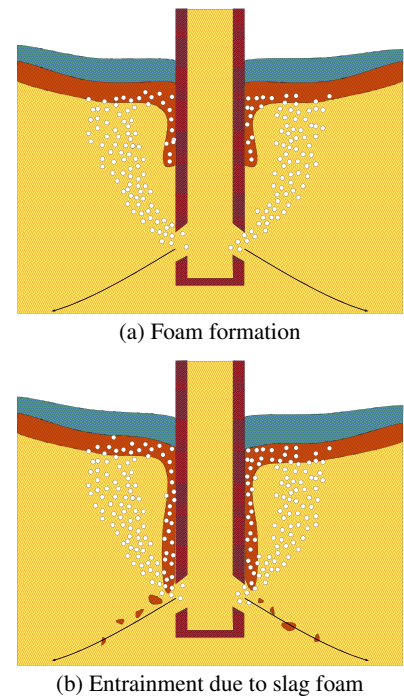


Figure 7. Slag foaming

The occurrence of the foam increases with decreasing bubble diameters, increasing strand width, increasing argon gas flow rate, increasing slag dynamic shear viscosity, decreasing slag mass density, and decreasing interfacial tension between the slag and steel⁵⁹. The critical argon flow rate that avoids slag foaming depends on the steel throughput; higher throughput causes smaller bubbles that have small inertia and follow the steel flow pattern⁵⁹. Other water model experiments¹⁹ observed that this critical argon flow rate decreases with increasing SEN flow rate, decreasing slag layer viscosity, aiming the SEN port angles more upward, and decreasing wettability between the SEN material and molten slag. Some plant trials⁵⁹ showed a reduction of pencil-pipe defects with reduced argon flow rate, but other plant trials⁷⁰ showed that the number of pencil blister defects correlates strongly with overall throughput and is insensitive to argon flow rate, SEN port angles, SEN port diameter, and SEN submergence depth.

As a bubble rises into and through the molten slag layer, a thin film of molten steel is caught between the bubble and the slag. If the bubble breaks through to the atmosphere, the film of steel will be trapped in the slag layer until gravity pulls it back into the melt, possibly bringing some slag with it^{71,72}, as shown in Figure 8. Physical model investigations revealed that the maximum depth the slag is carried downwards into the molten steel after bubble penetration into the slag layer was consistently about three times the bubble diameter⁷². Smaller bubbles were observed to not rupture the slag layer at all⁷¹. The physical properties of the fluids had almost no effect on this phenomenon, except that increasing the interfacial tension likely decreases the slag entrainment⁷². However, the flow inside the liquid slag layer^{73,74} and the constraint provided by the sintered slag layer⁷² forces the bubbles to move laterally towards the SEN or narrow face, somewhat mitigating the entrainment by this mechanism.

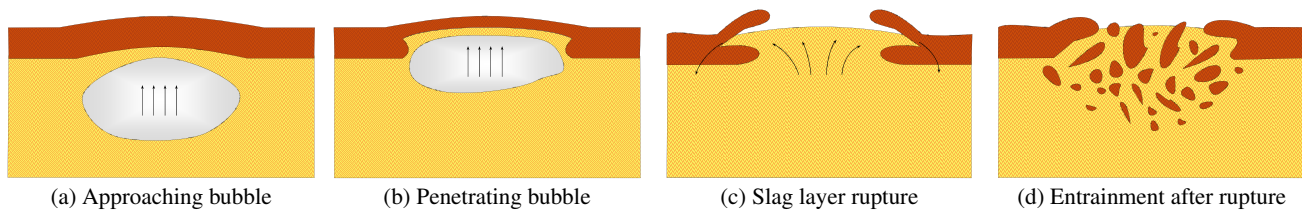


Figure 8. Entrainment by bubble penetration of slag layer

9. SLAG CRAWLING

A solid object submerged into a flowing liquid causes a pressure buildup on the windward (right) side and a corresponding pressure drop in the leeward (left) side, as illustrated in Figure 9a. In the presence of a free surface this pressure difference changes the position of the surface. Asymmetric flow in a continuous casting mold (see Section 5) can cause this situation to occur with the SEN. The low-pressure zone can draw liquid slag down along the leeward exterior surface of the SEN, as shown in Figure 9a. If this effect is severe enough, and the SEN depth is shallow enough, then the slag can crawl down the SEN walls and be carried away into the molten steel pool by the steel jet, as shown in Figure 9b.

Physical model experiments of flow past a circular cylinder in a rotating trough⁷⁵ investigated the effect of fluid properties on this entrainment mechanism. For casters with the ratio of SEN outer diameter to slab thickness, or “blockage factor,” between 0.4 and 0.6, the penetration depth h_p that the upper fluid crawls down the cylinder is

$$h_p = 1.9 \frac{C_{p,\max} \rho_u V_u^2 + C_{p,\min} \rho_\ell V_\ell^2}{g(\rho_\ell - \rho_u)} \quad (24)$$

where $C_{p,\max} = 1.0$ and $C_{p,\min} = 2.5$ are the maximum and minimum pressure coefficients for a circular SEN. The maximum pressure coefficient occurs at the forward stagnation point (windward side) and the minimum pressure coefficient occurs on the sides of the SEN, closest to the wide faces. For elliptical SENS, a numerical study⁷⁶ found that these pressure coefficients decrease with increasing aspect ratio as

$$C_{p,\max} = 1.376 - 0.0652a \quad (25a)$$

$$C_{p,\min} = 1.978 - 1.065 \ln(a), \quad (25b)$$

where the aspect ratio a is the ratio of the major diameter (parallel to the flow direction) to the minor diameter (perpendicular to the flow direction). Increasing the SEN aspect ratio reduces the slag penetration depth by reducing the pressure drop across the

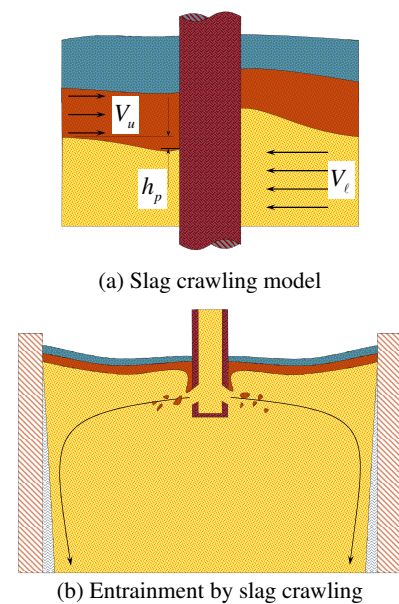


Figure 9. Slag crawling

SEN. This technique might help other flow-related defects by reducing the blockage factor, as is done commonly in thin-slab casters. Slag entrainment by this mechanism is avoided with the SEN immersion depth greater than the slag penetration depth⁷⁵. Note that these experiments were performed with materials with good wettability with the SEN; other work¹⁹ has shown that having poor wettability between the slag/oil layer and SEN refractory material increases the penetration depth by a factor of about 1.6.

The flow in these experiments was in the same direction on both sides of the SEN; in a caster the two flows oppose each other near the SEN, so Equation (24) may be an over-prediction of penetration depth in practice. However, the downward component of the molten steel flow near the SEN in double-roll flow can help the slag to crawl down the SEN. Additionally, the negative pressure zone often found in the top of SEN ports might assist the crawling action, though the negative pressure in the ports is not strong enough to cause entrainment by itself^{20,21} for reasonable immersion depths. Water model studies⁵⁹ observed a critical minimum immersion depth that causes immediate entrainment of a large number of small slag droplets, due to the combination of slag crawling, downward flow, and negative pressure at the top of the SEN ports. Slag crawling and the slag foaming mechanism discussed in Section 8 can act together to cause entrainment⁵⁹, but this effect is not reflected in Equation (24).

Water model studies^{19,71} observed that the oil layer was drawn downward via capillary action along the gas-filled spaces of the rough surface of the SEN, which was coated with a wax to decrease wettability. This capillary action may also be an entrainment mechanism in continuous casting molds.

10. TOP SURFACE STANDING WAVE INSTABILITY

Flow beneath a free liquid surface will create surface waves that become unstable if the local slope becomes too steep⁷⁷, *i.e.*, exceeding vertical, entraining one fluid into the other. This phenomenon is relevant at the top surface of the molten steel pool in continuous casting, where flow in the mold produces a standing wave at the surface. The standing wave also may become unstable if the vertical acceleration of the fluid is greater than the gravitational acceleration^{78,79}, although this appears not to be a problem in practice²⁵. This standing wave has a wavelength on the order of half of the mold width, in contrast to the smaller fluctuations discussed in Section 3. The top surface usually is raised near the narrow faces for double-roll flow patterns; however, sufficient argon flow rates can raise the top surface near the SEN¹⁹.

A numerical investigation⁷⁷ explored the stability of two-dimensional standing waves at the interface between two inviscid, irrotational, and incompressible fluids of different but uniform density in an infinite domain. The results of this study were reduced⁸⁰ to the height-to-wavelength stability criterion of

$$\left(\frac{h_{\text{wave}}}{\lambda}\right)_{\text{crit}} = 0.21 + 0.14r^2, \quad (26)$$

where h_{wave} is the wave height, defined for a caster as the vertical distance between the lowest point (trough) and highest point (crest) of the surface level, and λ is the wavelength, defined for a caster as the distance between the outer SEN wall and the narrow faces^{25,80,81}, although the value of λ does increase as SEN immersion depth h_{SEN} decreases⁸¹. As the density ratio ρ_u/ρ_ℓ decreases, the higher harmonics of the wave are damped out and the location of vertical slope shifts from the midpoint of the wave towards the crest⁷⁷. Physical⁸² and numerical⁸³ experiments show that a vortex forms at the wave node at lower height-to-wavelength ratios predicted by Equation (26), indicating that the stability of the wave is governed by shearing at the interface between the fluids, rather than the wave turning over⁷⁷.

Although derived for conditions different from a continuous caster, Equation (26) has been used to classify the critical wave height. A single-phase water model study¹⁷ gave the standing wave height as

$$h_{\text{wave}} = 0.577 \frac{V_{\text{port}}^2}{g} \frac{d_{\text{port}}}{L_{\text{URZ}}}, \quad (27)$$

where d_{port} is the diameter of the SEN ports, V_{port} is the velocity of the water or molten steel at the SEN ports, and L_{URZ} is a characteristic length of the upper recirculation zone, calculated from the geometry shown in Figure 10 as

$$L_{\text{URZ}} = h_{\text{SEN}} + \frac{1}{2}w_{\text{strand}} \tan\left(\theta_d - \frac{1}{2}\theta_j\right), \quad (28)$$

where h_{SEN} is the SEN immersion depth, w_{strand} is the strand width, θ_d is the jet discharge angle, and θ_j is the jet spread angle. The jet discharge angle is independent of flow rate⁸⁴, is independent of port width⁸⁴, aims more upward with increasing argon

flow rate⁴⁴, aims more downward with more downward lower-port angle^{44,84,85}, and the jet discharge angle is always more downward than the port angle^{84,85}. The jet discharge angle becomes closer to the lower port angle as the port height decreases and as the SEN wall thickness increases⁸⁴. The jet discharge angle also is a function of the port shape^{44,84}. The jet spread angle is independent of flow rate^{84,85}, independent of port width⁸⁴, and increases with more upward jet discharge angle⁸⁵. The jet impingement point was reported²⁰ to move downward about 25 mm to 50 mm for every 0.2 m/min increase in casting speed. A 2D numerical study²⁵ of another water model proposed

$$h_{\text{wave}} = 0.41 \frac{V_{\text{port}}^2}{g}. \quad (29)$$

Another prediction of the standing wave height using another water model²² is

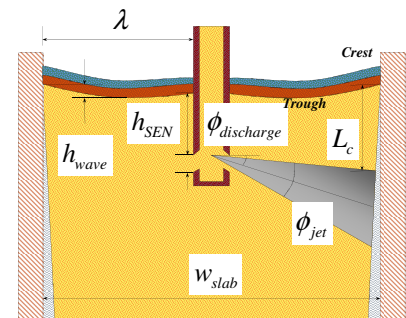
$$h_{\text{wave}} = 0.12 \frac{V_{\text{port}}^2}{g} \frac{d_{\text{port}}}{L_{\text{URZ}}}. \quad (30)$$

The effect of the slag layer on the surface standing wave is to increase the wave height. An oil-and-water physical model study⁸⁶ proposed that the wave height is

$$h_{\text{wave}} = 0.577 \frac{V_{\text{port}}^2}{g} \frac{d_{\text{port}}}{L_{\text{URZ}}} \frac{1}{1-r}. \quad (31)$$

A 2D numerical study⁸⁰ proposed that the wave height is

$$h_{\text{wave}} = 0.31 \frac{V_{\text{port}}^2}{g} \frac{d_{\text{port}}}{L_{\text{URZ}}} \frac{1+r}{1-r}. \quad (32)$$



(32) Figure 10. Top surface standing wave model description

The behavior of the top surface of the molten steel pool is a function of the flow pattern, which depends on throughput, SEN geometry and depth, and electromagnetic flow control systems. Using models based on the Froude number as in Equations (27) through (32) may help determine the functional relationship between quantities, but the numerical coefficients have limited applicability outside of the conditions for which they were derived, as indicated by different coefficients for the similar functional forms.

The models presented in Equations (27) through (32) show that the wave height h_{wave} increases with the dynamic head of the flow out of the SEN ports, V_{port}^2/g , because higher casting speeds or throughputs generally increase all velocities in the molten steel pool. Some researchers report²⁶ a linear relationship between wave height and casting speed, in contrast with the quadratic relationship given in the models presented in this section, while others report something in between^{81,87}. The wave height increases with increasing density ratio^{80,86}, decreasing SEN immersion depth^{17,81,86,87}, aiming the SEN port angles more upward^{17,26,86,87}, narrower strand widths^{1,17}, and narrower strand thicknesses¹. One study¹⁷ reports that the wave height increases with increasing SEN port diameter, while another⁸⁷ claims the reverse.

The initial numerical investigations^{25,80,81} into this entrainment mechanism assumed isothermal, room-temperature fluid flow and were not able to simulate the wave instability. Improvements to their interfacial tension calculations in a later 2D air-and-water simulation⁸³ of a water model¹⁷ successfully simulated the wave turning over and the resulting entrainment of air bubbles at the trough of the wave. A 3D single-phase numerical model of a thin-slab caster⁸⁷ that included the effect of temperature gradients and buoyancy showed a large increase in wave height because of the thermal effects. Other studies in thin-slab casters^{1,88} show that the presence of the shell (in the smaller liquid pool relative to thick-slab casters) affects all aspects of the flow pattern, including the top surface velocities and wave height.

The numerical study⁸³ with improved interfacial tension calculations showed a recirculating packet of fluid at the wave trough that disappeared after the instability event, which suggests that a vortex (with axis running between the wide faces) contributes to the instability of the interface. The highest surface velocities are found at the trough of the standing wave^{48,81,83}, which further supports the idea that the stability of the top surface is governed by the shearing stresses at the interface, discussed in Section 6, and not the wave-turnover mechanism (as was indicated in the original reference⁷⁷). However, none of the studies mentioned in this section investigated a real steel-slag system, and none of the computational models included all of the relevant physical phenomena in the same model.

11. TOP SURFACE BALDING

Some of the flow phenomena discussed above can be taken to the extreme of pushing the slag layer to the sides of the top surface, as illustrated in Figure 11a for excessive impinging flow upon the top surface⁴⁸. This phenomenon was termed “balding” of the surface, as it exposes molten steel to the atmosphere, if not the sintered and solid powder layers of the slag layer. This well-known phenomenon in ladle refining, there known as an “eye,” also can occur in continuous casting molds at high SEN flow rates, and the accompanying surface reoxidation forms inclusions such as alumina. Particles of mold powder can become entrained at the bald meniscus, especially if the bald spot coincides with the trough of the standing wave⁴⁸. Meniscus balding is prevented by having a minimum slag layer thickness of at least the size of the standing wave height⁸⁶, such as predicted from one of Equations (27) through (32). Meniscus balding also can be caused by high argon flow rates¹⁸, as illustrated in Figure 11b.

12. DETERMINING THE SAFE OPERATING WINDOW

Designing a caster to avoid mold slag entrapment requires the careful selection of many different parameters to find the window of stable, entrapment-free operation. The casting conditions must be chosen to avoid simultaneously each of the above mechanisms.

Like in most engineering problems, the prevention of entrapment involves many trade-offs. For example, the choice of slag layer properties must balance the conflicting needs to use the slag to capture inclusions, which requires lower interfacial tension, and to prevent shear-layer instability, which requires higher interfacial tension. Preventing entrapment by both top surface fluctuations and shear-layer instability requires control of the top surface velocities with proper selection of SEN parameters and electromagnetic flow control settings. However, the meniscus temperatures must remain high enough to prevent the formation of hooks.

The models presented in this article can be used together as design tools or to evaluate the results of physical or numerical models of flow in a caster. Note that the different mechanisms can act together, which affects the entrapment criteria. For example, the critical velocity condition for a given mechanism can be exceeded with asymmetric flow (which also creates entrapment by vortex formation), even though the symmetric time-averaged flow conditions yield no risk of entrapment. Uneven SEN clogging often is responsible for such asymmetric flow patterns, with top surface velocities easily doubling their unclogged values²¹; see also the discussion of asymmetric flow in Section 9.

13. CONCLUSIONS

Many studies have been performed over the years to investigate mold slag entrapment, which is one of the main sources of inclusion defects in the continuous casting of steel. This review article identified nine distinct mechanisms responsible for mold slag entrapment: top surface level fluctuations, meniscus freezing, vortexing, shear-layer instability, narrow-face spout impingement upon the top surface, and argon bubble interactions. The slag layer can also crawl down the SEN, but this effect is an issue only at very shallow submergence depths, or when combined with the slag foaming with argon bubbles. Another mechanism, the instability of the top-surface standing wave, appears unimportant because shear-layer instability occurs more easily. Extreme flow conditions result in the “balding” of the top surface and should be avoided. The various simple models available to estimate these nine mechanisms are summarized in this article, which can be used together to evaluate the quality of flow patterns found from physical or numerical models of flow in the continuous casting process.

ACKNOWLEDGMENTS

The authors gratefully acknowledge the financial support of the member companies of the Continuous Casting Consortium at the University of Illinois at Urbana-Champaign. The authors thank Junya Iwasaki of Nippon Steel Company for translation of some of the references.

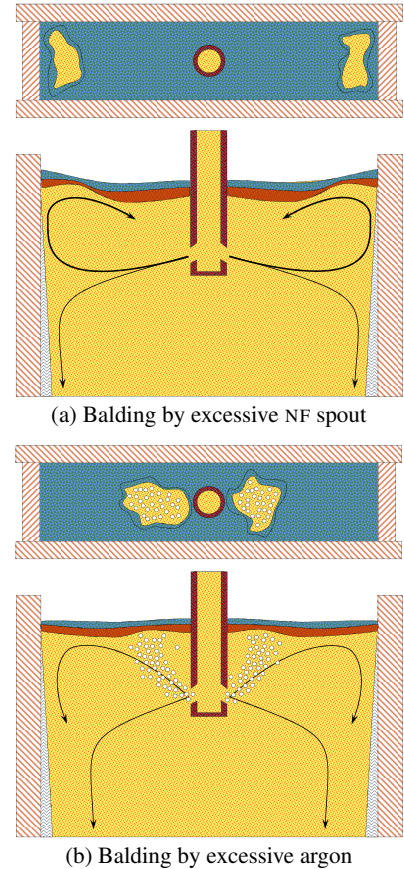


Figure 11. Top surface balding

REFERENCES

- [1] R. Chaudhary, B. T. Rietow, and B. G. Thomas, "Differences between physical water models and steel continuous casters: A theoretical evaluation," in *Proceedings of the Materials Science and Technology Conference*, pp. 1090–1101, ACerS/AIST/ASM/TMS, 2009.
- [2] Q. Yuan and B. G. Thomas, "Transport and entrapment of particles in continuous casting of steel," in *Proceedings of 3rd International Congress on Science and Technology of Steelmaking*, pp. 745–762, The Association for Iron and Steel Technology, 2005.
- [3] Q. Yuan and B. G. Thomas, "Transport and entrapment of particles in continuous casting of steel," in *Proceedings of Modeling of Casting, Welding, and Advanced Solidification Processes XI*, pp. 745–752, The Minerals, Metals, and Materials Society, 2006.
- [4] G.-G. Lee, H.-J. Shin, B. G. Thomas, and S.-H. Kim, "Asymmetric multi-phase fluid flow and particle entrapment in a continuous casting mold," in *Proceedings of AISTech*, vol. 2, pp. 63–73, The Association for Iron and Steel Technology, 2008.
- [5] S. Kunstreich and P. H. Dauby, "Effect of liquid steel flow pattern on slab quality and the need for dynamic electromagnetic control in the mould," *Ironmaking and Steelmaking*, vol. 32, no. 1, pp. 80–86, 2005.
- [6] A. W. Cramb and I. Jimbo, "Interfacial considerations in continuous casting," *ISS Transactions*, vol. 11, pp. 67–79, 1990.
- [7] A. W. Cramb, Y. Chung, J. Harman, A. Sharan, and I. Jimbo, "The slag/metal interface and associated phenomena," *Iron and Steelmaker*, vol. 24, no. 3, pp. 77–83, 1997.
- [8] D. Bouris and G. Bergeles, "Investigation of inclusion re-entrainment from the steel-slag interface," *Metallurgical and Materials Transactions B*, vol. 29, no. 3, pp. 641–649, 1998.
- [9] J. Strandh, K. Nakajima, R. Eriksson, and P. Jönsson, "A mathematical model to study liquid inclusion behavior at the steel-slag interface," *ISIJ International*, vol. 45, no. 12, pp. 1838–1847, 2005.
- [10] C. Ojeda, B. G. Thomas, J. Barco, and J. Arana, "Model of thermal-fluid flow in the meniscus region during an oscillation cycle," in *Proceedings of AISTech*, vol. 2, pp. 269–283, The Association for Iron and Steel Technology, 2007.
- [11] J. Sengupta, C. Ojeda, and B. G. Thomas, "Thermal-mechanical behaviour during initial solidification in continuous casting: Steel grade effects," *International Journal of Cast Metals Research*, vol. 22, no. 1–4, pp. 8–14, 2009.
- [12] R. Liu, B. G. Thomas, L. Kalra, T. Bhattacharya, and A. Dasgupta, "Slide-gate dither effects on transient flow and mold level fluctuations," in *Proceedings of AISTech*, The Association for Iron and Steel Technology, 2013.
- [13] M. Javurek, M. Thumfart, K. Rieger, and M. Hirschmanner, "Mathematical mould level model based on numerical simulations and water model experiments," in *Proceedings of the 6th European Conference on Continuous Casting*, 2008.
- [14] J. Kubota, K. Okimoto, A. Shirayama, and H. Murakami, "Meniscus flow control in the mold by travelling magnetic field for high speed slab caster," in *7th Steelmaking Conference Proceedings*, pp. 233–241, The Iron and Steel Society, 1991.
- [15] T. Teshima, M. Osame, K. Okimoto, and Y. Nimura, "Improvement of surface property of steel at high casting speed," in *71st Steelmaking Conference Proceedings*, pp. 111–118, The Iron and Steel Society, 1988.
- [16] H. Nakato, K. Saito, Y. Oguchi, N. Namura, and K. Sorimachi, "Surface quality improvement of continuously cast blooms by optimizing solidification in early stage," in *70th Steelmaking Conference Proceedings*, pp. 427–431, The Iron and Steel Society, 1987.
- [17] D. Gupta and A. K. Lahiri, "Water-modeling study of the surface disturbances in continuous slab caster," *Metallurgical and Materials Transactions B*, vol. 25, no. 2, pp. 227–233, 1994.
- [18] D. J. Harris and J. D. Young, "Water modeling – a viable production tool," in *65th Steelmaking Conference Proceedings*, pp. 3–16, The Iron and Steel Society, 1982.
- [19] Z. Wang, K. Mukai, Z. Ma, M. Nishi, H. Tsukamoto, and F. Shi, "Influence of injected argon gas on the involvement of the mold powder under different wettabilities between porous refractory and molten steel," *ISIJ International*, vol. 39, no. 8, pp. 795–803, 1999.
- [20] Y. H. Wang, "A study of the effect of casting conditions on fluid flow in the mold using water modelling," in *73rd Steelmaking Conference Proceedings*, pp. 473–480, The Iron and Steel Society, 1990.
- [21] Q. He, G. Evans, R. Serje, and T. Jaques, "Fluid flow and mold slag entrapment in the continuous twin-slab casting mould," in *Proceedings of AISTech*, vol. 2, pp. 573–588, The Association for Iron and Steel Technology, 2009.
- [22] B. S. Moghaddam, E. Steinmetz, and P. R. Scheller, "Interaction between the flow condition and the meniscus disturbance in the continuous slab caster," in *Proceedings of the International Congress on the Science and Technology of Steelmaking*, vol. 3, pp. 911–920, The Association for Iron and Steel Technology, 2005.
- [23] P. Andrzejewski, K.-U. Köhler, and W. Pluschkell, "Model investigations on the fluid flow in continuous casting moulds of wide dimensions," *Steel Research*, vol. 63, no. 6, pp. 242–246, 1992.
- [24] A. Matsushita, K. Isogami, M. Temma, T. Ninomiya, and K. Tsutsumi, "Direct observation of molten steel meniscus in CC mold during casting," *Transactions of the ISIJ*, vol. 28, no. 7, pp. 531–534, 1988.
- [25] G. A. Panaras, A. Theodorakakos, and G. Bergeles, "Numerical investigation of the free surface in a continuous steel casting mold," *Metallurgical and Materials Transactions B*, vol. 29, no. 5, pp. 1117–1126, 1998.
- [26] T. Honeyands and J. Herbertson, "Flow dynamics in thin slab caster moulds," *Steel Research*, vol. 66, no. 7, pp. 287–293, 1995.
- [27] R. Chaudhary, B. G. Thomas, and S. P. Vanka, "Effect of electromagnetic ruler braking (EMBr) on transient turbulent flow in continuous slab casting using large eddy simulations," *Metallurgical and Materials Transactions B*, vol. 43, no. 3, pp. 532–553, 2012.
- [28] S. Kunstreich, P. H. Dauby, S.-K. Baek, and S.-M. Lee, "Multi-mode ems in thick slab caster molds and effect on coil quality and machine performance," in *Proceedings of the 5th European Conference on Continuous Casting*, 2005.

- [29] K. Cukierski and B. G. Thomas, "Flow control with local electromagnetic braking in continuous casting of steel," *Metallurgical and Materials Transactions B*, vol. 39, no. 1, pp. 94–107, 2008.
- [30] H. Nakamura, S. Kohira, J. Kubota, T. Kondo, M. Suzuki, , and Y. Shiratani, "Technology for production of high quality slab at high speed casting," in *75th Steelmaking Conference Proceedings*, pp. 409–415, The Iron and Steel Society, 1992.
- [31] J. Kubota, K. Okimoto, M. Suzuki, A. Shirayama, and T. Masaoka, "Mechanism of level fluctuation and mold powder catching in slab continuous casting at high speeds," in *Proceedings of the 6th International Iron and Steel Congress*, vol. 3, pp. 356–363, The Iron and Steel Institute of Japan, 1990.
- [32] G.-G. Lee, B. G. Thomas, S.-H. Kim, H.-J. Shin, S.-K. Baek, C.-H. Choi, D.-S. Kim, and S.-J. Yu, "Microstructure near corners of continuous-cast steel slabs showing three-dimensional frozen meniscus at hooks," *Acta Materialia*, vol. 55, no. 20, pp. 6705–6712, 2007.
- [33] J. Sengupta, B. G. Thomas, H.-J. Shin, G.-G. Lee, and S.-H. Kim, "A new mechanism of hook formation during continuous casting of ultra-low-carbon steel slabs," *Metallurgical and Materials Transactions A*, vol. 37, no. 5, pp. 1597–1611, 2006.
- [34] S.-M. Cho, G.-G. Lee, S.-H. Kim, R. Chaudhary, O.-D. Kwon, and B. G. Thomas, "Effect of stopper-rod misalignment on asymmetric flow and vortex formation in steel slab casting," in *Jim Evans Honorary Symposium, in Proceedings of The Minerals, Metals, and Materials Society 139th Annual Meeting*, pp. 71–77, The Minerals, Metals, and Materials Society, 2010.
- [35] N. Kasai and M. Iguchi, "Water-model experiment on melting powder trapping by vortex in the continuous casting mold," *ISIJ International*, vol. 47, no. 7, pp. 982–987, 2007.
- [36] B. Li, T. Okane, , and T. Umeda, "Modeling of biased flow phenomena associated with the effects of static magnetic-field application and argon gas injection in slab continuous casting of steel," *Metallurgical and Materials Transactions B*, vol. 32, no. 6, pp. 1053–1066, 2001.
- [37] B. Li and F. Tsukihashi, "Vortexing flow patterns in a water model of slab continuous casting mold," *ISIJ International*, vol. 45, no. 1, pp. 30–36, 2005.
- [38] Q. He, "Observations of vortex formation in the mould of a continuous slab caster," *ISIJ International*, vol. 33, no. 2, pp. 343–345, 1993.
- [39] H. Bai and B. G. Thomas, "Effects of clogging, argon injection, and continuous casting conditions on flow and air aspiration in submerged entry nozzles," *Metallurgical and Materials Transactions B*, vol. 32, no. 4, pp. 707–722, 2001.
- [40] S. Mahmood, "Efficient modeling of flow asymmetries and particle entrapment in nozzle and mold during continuous casting of steel slabs," Master's thesis, The University of Illinois at Urbana-Champaign, 2006.
- [41] L. Zhang, Y. Wang, and X. Zuo, "Flow transport and inclusion motion in steel continuous-casting mold under submerged entry nozzle clogging condition," *Metallurgical and Materials Transactions B*, vol. 39, no. 4, pp. 534–550, 2008.
- [42] R. Chaudhary, G.-G. Lee, B. G. Thomas, S.-M. Cho, S.-H. Kim, and O.-D. Kwon, "Effect of stopper-rod misalignment on fluid flow in continuous casting of steel," *Metallurgical and Materials Transactions B*, vol. 42, pp. 300–315, 2011.
- [43] H. Bai and B. G. Thomas, "Turbulent flow of liquid steel and argon bubbles in slide-gate tundish nozzles: Part I. model development and validation," *Metallurgical and Materials Transactions B*, vol. 32, no. 2, pp. 253–267, 2001.
- [44] H. Bai and B. G. Thomas, "Turbulent flow of liquid steel and argon bubbles in slide-gate tundish nozzles: Part II. effect of operation conditions and nozzles design," *Metallurgical and Materials Transactions B*, vol. 32, no. 2, pp. 269–284, 2001.
- [45] M. Gebhard, Q. He, and J. Herbertson, "Vortexing phenomena in continuous slab casting moulds," in *76th Steelmaking Conference Proceedings*, pp. 441–446, The Iron and Steel Society, 1993.
- [46] B. Li and F. Tsukihashi, "Effects of electromagnetic brake on vortex flows in this slab continuous casting mold," *ISIJ International*, vol. 46, no. 12, pp. 1833–1838, 2006.
- [47] G. Kastner, W. Brandstätter, B. Kaufmann, C. Wassermayr, and M. Javurek, "Numerical study on mould powder entrapment caused by vortexing in a continuous casting process," *Steel Research International*, vol. 77, no. 6, pp. 404–408, 2006.
- [48] D. Gupta and A. K. Lahiri, "Cold model study of slag entrainment into liquid steel in continuous slab caster," *Ironmaking and Steelmaking*, vol. 23, no. 4, pp. 361–363, 1996.
- [49] K. Tsutsumi, K. Watanabe, M. Suzuki, M. Nakada, and T. Shiomi, "Effect of properties of mold powder entrapped in molten steel in a continuous casting process," in *VII International Conference on Molten Slags, Fluxes, and Salts*, pp. 803–806, The South African Institute of Mining and Metallurgy, 2004.
- [50] K. Watanabe, K. Tsutsumi, M. Suzuki, M. Nakada, and T. Shiomi, "Effect of properties of mold powder entrapped into molten steel in a continuous casting process," *ISIJ International*, vol. 49, no. 8, pp. 1161–1166, 2009.
- [51] H. L. F. von Helmholtz, "Über discontinuierliche fließbewegungen," *Monatsberichte der Königlich Preussische Akademie der Wissenschaften zu Berlin*, vol. 23, pp. 215–228, 1868.
- [52] W. Thomson, "Hydrokinetic solutions and observations," *Philosophical Magazine*, vol. 42, no. 281, pp. 362–377, 1871.
- [53] L. M. Milne-Thomson, *Theoretical Hydrodynamics*. London: Macmillan Press, 5 ed., 1968. Example XV.17.
- [54] M. Iguchi, J. Yoshida, T. Shimizu, and Y. Mizuno, "Model study on the entrapment of mold powder into molten steel," *ISIJ International*, vol. 40, no. 7, pp. 685–691, 2000.
- [55] T. Funada and D. D. Joseph, "Viscous potential flow analysis of kelvin-helmholtz instability in a channel," *Journal of Fluid Mechanics*, vol. 445, pp. 263–283, 2001.
- [56] S. Chandrasekhar, *Hydrodynamic and Hydromagnetic Stability*, pp. 481–514. Oxford: Clarendon Press, 1961.
- [57] P.-R. Cha and J.-K. Yoon, "The effect of a uniform direct current magnetic field on the stability of a stratified liquid flux/molten steel system," *Metallurgical and Materials Transactions B*, vol. 31, no. 2, pp. 317–326, 2000.
- [58] J. M. Harman and A. W. Cramb, "A study of the effect of fluid physical properties upon droplet emulsification," in *79th Steelmaking Conference Proceedings*, pp. 773–784, The Iron and Steel Society, 1996.

- [59] W. H. Emling, T. A. Waugaman, S. L. Feldbauer, and A. W. Cramb, "Subsurface mold slag entrainment in ultra low carbon steels," in *77th Steelmaking Conference Proceedings*, pp. 371–379, The Iron and Steel Society, 1994.
- [60] S. Asai, "Fluid flow and mass transfer in a refining process by use of stirring," in *Proceedings of the 100th and 101st Nishiyama Memorial Lecture*, pp. 65–100, The Iron and Steel Institute of Japan, 1984.
- [61] H. Yuyama, S. Kashio, S. Tsuneoka, K. Ohtaki, and N. Matsuda, "Development of bath level variation detector in CC mold," *Tetsu-to-Hagane*, vol. 72, no. 12, p. S1018, 1986.
- [62] R. Hagemann, R. Schwarze, H. P. Heller, and P. R. Scheller, "Model investigations on the stability of the steel-slag interface in continuous-casting process," *Metallurgical and Materials Transactions B*, vol. 44, no. 1, pp. 80–90, 2013.
- [63] J. Savolainen, T. Fabritius, and O. Mattila, "Effect of fluid physical properties on the emulsification," *ISIJ International*, vol. 49, no. 1, pp. 29–36, 2009.
- [64] K. Krishnapisharody and G. A. Irons, "Modeling and analysis of slag droplet formation in ladle metallurgy practice," in *Proceedings of AISTech*, vol. 2, pp. 1243–1252, The Association for Iron and Steel Technology, 2008.
- [65] K. Krishnapisharody and G. A. Irons, "Model studies on slag droplet generation in gas-stirred ladles," in *EPD Congress 2008, in Proceedings of The Minerals, Metals, and Materials Society 138th Annual Meeting*, pp. 293–302, The Minerals, Metals, and Materials Society, 2008.
- [66] K. Krishnapisharody and G. A. Irons, "Numerical simulation of droplet generation of the buoyant phase in two-phase liquid baths," in *EPD Congress 2008, in Proceedings of The Minerals, Metals, and Materials Society 138th Annual Meeting*, pp. 311–322, The Minerals, Metals, and Materials Society, 2008.
- [67] Z. Xiao, Y. Peng, and C. Liu, "Modelling study of the entrapment phenomena at the slag-metal interface in the gas-stirred ladle," *Chinese Journal of Metal Science and Technology*, vol. 3, pp. 187–193, 1987.
- [68] T. Wei and F. Oeters, "A model test for emulsion in gas-stirred ladles," *Steel Research*, vol. 63, no. 2, pp. 60–68, 1992.
- [69] B. G. Thomas, X. Huang, and R. C. Sussman, "Simulation of argon gas flow effects in a continuous slab caster," *Metallurgical and Materials Transactions B*, vol. 25, no. 4, pp. 527–547, 1994.
- [70] J. Knoepke, M. Hubbard, J. Kelly, R. Kittridge, and J. Lucas, "Pencil blister reduction at inland steel company," in *77th Steelmaking Conference Proceedings*, pp. 381–388, The Iron and Steel Society, 1994.
- [71] T. Watanabe and M. Iguchi, "Water model experiments on the effect of an argon bubble on the meniscus near the immersion nozzle," *ISIJ International*, vol. 49, no. 2, pp. 182–188, 2009.
- [72] S. Yamashita and M. Iguchi, "Mechanism of mold powder entrapment caused by large argon bubble in continuous casting mold," *ISIJ International*, vol. 41, no. 12, pp. 1529–1531, 2001.
- [73] R. M. McDavid and B. G. Thomas, "Flow and thermal behavior of the top surface flux/powder layers in continuous casting molds," *Metallurgical and Materials Transactions B*, vol. 27, no. 4, pp. 672–685, 1996.
- [74] B. Zhao, S. P. Vanka, and B. G. Thomas, "Numerical study of flow and heat transfer in a molten flux layer," *International Journal of Heat and Fluid Flow*, vol. 26, no. 1, pp. 105–118, 2005.
- [75] J. Yoshida, T. Ohmi, and M. Iguchi, "Cold model study on the effects of density difference and blockage factor on mold powder entrapment," *ISIJ International*, vol. 45, no. 8, pp. 1160–1164, 2005.
- [76] Y. Ueda, T. Kida, and M. Iguchi, "Unsteady pressure coefficient around an elliptic immersion nozzle," *ISIJ International*, vol. 44, no. 8, pp. 1403–1409, 2004.
- [77] J. W. Rottman, "Steep standing waves at a fluid interface," *Journal of Fluid Mechanics*, vol. 124, pp. 283–306, 1982.
- [78] W. G. Penney and A. T. Price, "Finite periodic stationary gravity waves in a perfect liquid," *Philosophical Transactions of the Royal Society of London A*, vol. 244, no. 882, pp. 254–284, 1952.
- [79] L. W. Schwartz and A. K. Whitney, "A semi-analytic solution for nonlinear standing waves in deep water," *Journal of Fluid Mechanics*, vol. 107, pp. 147–171, 1981.
- [80] A. Theodorakakos and G. Bergeles, "Numerical investigation of the interface in a continuous steel casting mold water model," *Metallurgical and Materials Transactions B*, vol. 29, no. 6, pp. 1321–1327, 1998.
- [81] J. Anagnostopoulos and G. Bergeles, "Three-dimensional modeling of the flow and the interface surface in a continuous casting mold model," *Metallurgical and Materials Transactions B*, vol. 30, no. 6, pp. 1095–1105, 1999.
- [82] S. A. Thorpe, "On standing internal gravity waves of finite amplitude," *Journal of Fluid Mechanics*, vol. 32, no. 3, pp. 489–528, 1968.
- [83] S. K. Dash, S. S. Mondal, and S. K. Ajmani, "Mathematical simulation of surface wave created in a mold due to submerged entry nozzle," *International Journal of Numerical Methods for Heat and Fluid Flow*, vol. 14, no. 5, pp. 606–632, 2004.
- [84] F. M. Najjar, B. G. Thomas, and D. E. Hershey, "Numerical study of steady turbulent flow through bifurcated nozzles in continuous casting," *Metallurgical and Materials Transactions B*, vol. 26, no. 4, pp. 749–765, 1995.
- [85] D. Gupta and A. K. Lahiri, "Water modelling study of the jet characteristics in a continuous casting mould," *Steel Research*, vol. 63, no. 5, pp. 201–204, 1992.
- [86] D. Gupta and A. K. Lahiri, "Cold model study of the surface profile in a continuous slab casting mold: Effect of second phase," *Metallurgical and Materials Transactions B*, vol. 27, no. 4, pp. 695–697, 1996.
- [87] M. Kamal and Y. Sahai, "Modeling of melt flow and surface standing waves in a continuous casting mold," *Steel Research International*, vol. 76, no. 1, pp. 44–52, 2005.
- [88] B. Rietow, "Fluid velocity simulation and measurement in thin slab casting," Master's thesis, The University of Illinois at Urbana–Champaign, 2007.